Transannularly Conjugated Tetrameric Perylene Diimide Acceptors Containing [2.2]Paracyclophane for Non-fullerene Organic Solar Cells

SCHOLARONE™
Manuscripts

Transannularly Conjugated Tetrameric Perylene Diimide Acceptors Containing [2.2]Paracyclophane for Non-fullerene Organic Solar Cells

Han Yu,[‡a] Lingeswaran Arunagiri,[‡a] Lin Zhang,[d] Jiachen Huang,[a] Wei Ma,[*c] Jianquan Zhang,[*a] He Yan[*ab]

[a] Department of Chemistry, Hong Kong University of Science and Technology (HKUST), Clear Water Bay, Kowloon, Hong Kong SAR, P. R. China

[b] Hong Kong University of Science and Technology-Shenzhen Research Institute, No. 9, Yuexing 1st RD, Hi-tech Park, Nanshan, Shenzhen 518057, P. R. China

[c] State Key Laboratory for Mechanical Behavior of Materials, Xi'an Jiaotong University, Xi'an, 710049, P. R. China

[d] Hunan Key Laboratory for Super Microstructure and Ultrafast Process, School of Physics and Electronics, Central South University, Changsha 410083, China

‡ These authors contributed equally to this work.

Correspongding Author

He Yan (hyan@ust.hk)

Jianquan Zhang (jzhangbn@connect.ust.hk)

Wei Ma (msewma@xjtu.edu.cn)

Abstract

Core engineering of perylene diimide (PDI)-based small molecular acceptors has played a critical role in boosting the device performances in the field of organic solar cells (OSCs). In this work, two regio-isomeric PDI-based acceptors (named oCP-FPDI4 and pCP-FPDI4) based on a novel [2.2]paracyclophane core were designed and synthesized. Due to the subtle variations in the functionalization positions on the [2.2]paracyclophane moiety, the two PDI acceptors exhibit different molecular geometry and absorption properties. When blended with the donor polymer named P3TEA, oCP-FPDI4 and pCP-FPDI4 showed dramatic differences in photovoltaic performances (2.42% vs. 9.06%). In-depth studies on nano-scale morphology of the respective blend films revealed that the P3TEA:pCP-FPDI4 blend exhibited suitable phase segregation, thus contributing to the better charge dissociation and less charge recombination. The marked variations in photovoltaic performances between oCP-FPDI4 and pCP-FPDI4 highlight the importance of regulating the spatial orientations in the design of PDI-based acceptors using cyclophane derivatives.

1. Introduction

Over the past few years, organic solar cells (OSCs) have been considered as one of the promising alternatives to the traditional inorganic solar cells, due to their low cost, light weight and mechanical flexibility.[1-6] Enormous efforts have been devoted to developing non-fullerene electron acceptors, especially small molecular acceptors (SMAs).[7-13] Among various types of non-fullerene acceptors, perylene diimides (PDI) derivatives are one of the most investigated families with readily tuned energy levels and absorption, excellent stability and also high electron-transporting ability.[14-17] Most progress made in the development of novel PDI-based SMAs has been propelled by rational design of the aromatic central cores to construct PDI oligomers having twisted molecular geometry, either with non-fused[18-30] or ring-fused structure[7, 31-41]. Fine-tuning the spatial orientation of PDI subunits can be achieved by proper functionalization of aromatic central cores, which is the key to resolve the long-standing dilemma between suitable phase segregation and efficient charge transport of PDI-based SMAs. So far, PDI-based OSC devices have obtained power conversion efficiencies (PCEs) surpassing 10% through substantial research work on core engineering.[7, 42]

Among numerous building blocks for constructing functional π systems, the cyclophanes family (CP, **Figure 1**) containing two or more aromatic rings locked into a face-to-face geometry by certain linkages is of great research interest, especially in the field of supramolecular chemistry and optoelectronic materials.[43-45] The functional materials based on cyclophanes exhibit unique optoelectronic properties owing to their transannular π-π interactions, or so-called through-space conjugation, between the cofacially π-stacked aromatic systems. For example, in a [2.2]paracyclophane molecule the distance between two phenyl rings is 3.10 Å, while the typical π-π stacking distance of graphite is 3.35 Å. The shorter π-π stacking distance in [2.2]paracyclophane leads to strong orbital overlap, thus enabling π electron delocalization through the two phenyl rings. As a result, charge transport and energy transfer occur efficiently within the

3

molecules containing [2.2]paracyclophane as the skeleton via not only through-bond but also through-space channels.[46-51] In addition to these intriguing properties, the synthetic diversity and convenience of [2.2]paracyclophane derivatives provides an opportunity to investigate the structure-property relationships in terms of spatial orientations and functionalization, as through-space conjugation is highly sensitive to molecular geometry and electronic structures. Whereas, although cyclophane chemistry has been developed rapidly into a vibrant and multifaceted field of study, cyclophane derivatives have not yet been applied as a building block for constructing electron acceptors in the OSC field to the best of our knowledge.

In this work, we for the first time examined the use of [2.2]paracyclophane for constructing electron acceptors for OSC operations. Two novel tetrathienyl [2.2]paracyclophane constitutional isomers, which differ in the functionalization positions of the cyclophane moiety (i.e., ortho- and para-positions), were designed and synthesized (**Figure 1**). After ring fusion of four PDI wings, two tetrameric PDI-based SMAs named *o*CP-FPDI4 and *p*CP-FPDI4 were obtained and systematically studied. When blending with a donor polymer P3TEA, both PDI-based SMAs yielded high open-circuit voltages (V_{OC}) of up to 1.17 V associated with voltage losses as low as 0.49 V. However, the *p*CP-FPDI4-based devices showed dramatically enhanced short-circuit current density (J_{SC}) and fill factor (FF) compared with the *o*CP-FPDI4-based ones, resulting in the highest PCE of 9.06%. Morphological studies revealed that one of the prime reasons for the higher performances of the *p*CP-FPDI4-based devices is the suitable nano-scale phase segregation formed in the P3TEA:*p*CP-FPDI4 blends, leading to suppressed charge recombination and more efficient charge dissociation. Our work provides insights into the constitutional isomeric effects of the [2.2]paracyclophane-PDI electron acceptors and highlights the potential applications of cyclophane derivatives in the design of photo-active materials for OSC devices.

4
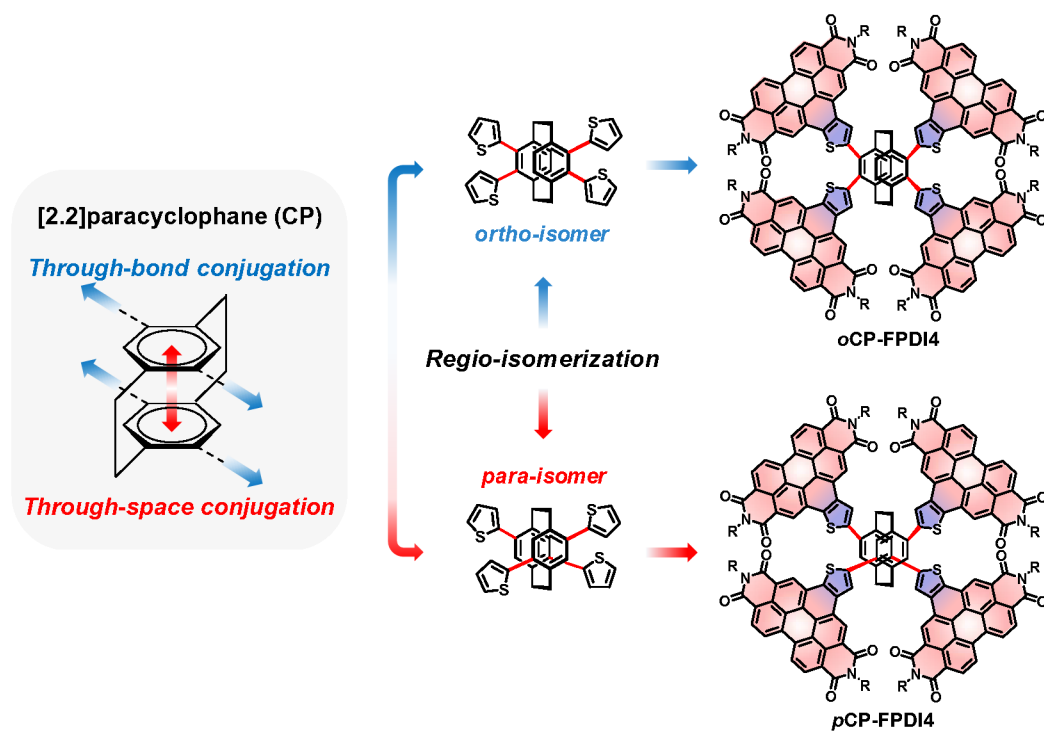
Figure 1. Chemical structure of [2.2]paracyclophane (CP) and the isomeric PDI-based derivatives (*o*CP-FPDI4 and *p*CP-FPDI4).

2. Results and Discussions
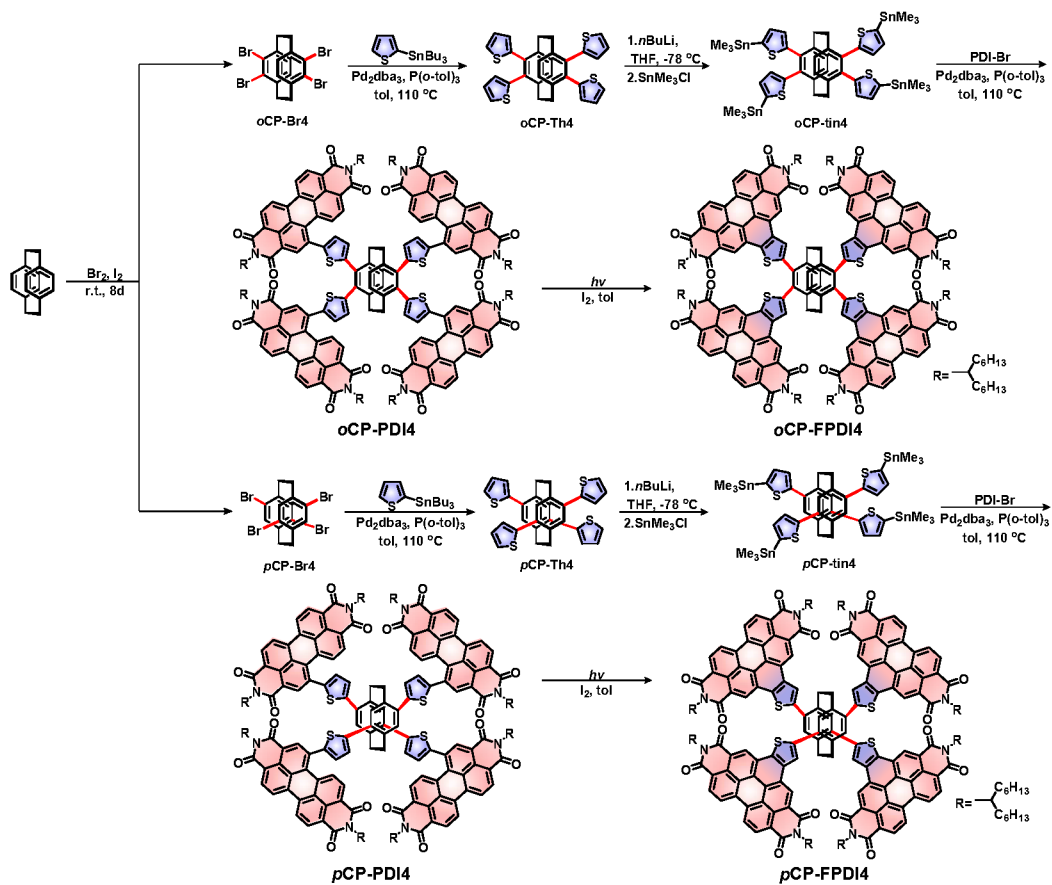
Scheme 1. Synthetic route to *o*CP-FPDI4 and *p*CP-FPDI4.

The synthetic route to *o*CP-FPDI4 and *p*CP-FPDI4 is illustrated in **Scheme 1**. Starting from bromination of [2.2]paracyclophane, two regio-isomeric tetrebromo-[2.2]paracyclophane, *o*CP-Br$_4$ and *p*CP-Br$_4$ were obtained. *o*CP-Br$_4$ has two bromine atoms at the ortho-positions of each benzene ring, while *p*CP-Br$_4$ has the bromine atoms at the para-positions. The *o*CP-Br$_4$ and *p*CP-Br$_4$ cores were subsequently subjected to a three-step procedure, i.e., Stille cross-coupling with 2-(tributylstannyl)thiophene, stannylation and Stille cross-coupling with C$_6$-PDI-Br, to prepare the non-fused tetrameric PDI precursors, *o*CP-PDI4 and *p*CP-PDI4. Finally, the precursors were dissolved in toluene with a catalytic amount of I$_2$ and exposed to irradiation under a

500 W mercury lamp to yield the ring-fused tetrameric PDI acceptors, *o*CP-FPDI4 and *p*CP-FPDI4, in decent yields. All the compounds were unambiguously characterized by ^{1}H NMR, ^{13}C NMR and mass spectra, and summarized in the Supporting Information. The thermal decomposition temperature (T_d) are measured to be 306 °C for both PDI molecules from thermogravimetric analysis (TGA, at 5% weight loss, **Figure S1**).

To investigate the isomeric effects between *o*CP-FPDI4 and *p*CP-FPDI4, theoretical calculations were performed using density-functional theory (DFT) with B3LYP/6-31(d,p) basis set to study the molecular geometries and frontier molecular orbitals (FMO). The long branched alkyl chains were replaced by methyl groups to simplify the calculations. As shown in **Figure 2a** and **2b**, both *o*CP-FPDI4 and *p*CP-FPDI4 exhibit twisted optimized molecular geometry. However, the PDI units of *o*CP-FPDI4 attached to the ortho-positions apparently show larger steric hindrance than those of *p*CP-FPDI4 at the para-positions. As a result, the dihedral angles between the PDI units and the [2.2]paracyclophane core are dramatically different between *o*CP-FPDI4 (64.8°) and *p*CP-FPDI4 (24.2°), which will alter the conjugation along the molecular skeletons and thus the FMO of the molecules. As expected, both HOMO and LUMO of *o*CP-FPDI4 locate only on the four PDI units with a gap lying on the [2.2]paracyclophane core that may disrupt the electron transfer channel (**Figure 2c**). In contrast, the HOMO and LUMO of *p*CP-FPDI4 distribute through the entire molecular backbone, indicating a better conjugation between the [2.2]paracyclophane core and the PDI units (**Figure 2d**). More interestingly, through-space conjugation between the two benzene rings of *p*CP-FPDI4 can be observed. The better conjugation of *p*CP-FPDI4 is supported by the smaller HOMO-LUMO gap of *p*CP-FPDI4 (-5.73/-3.35 eV) than that of *o*CP-FPDI4 (-6.05/-3.35 eV), considering the two isomeric molecules have the same composition.
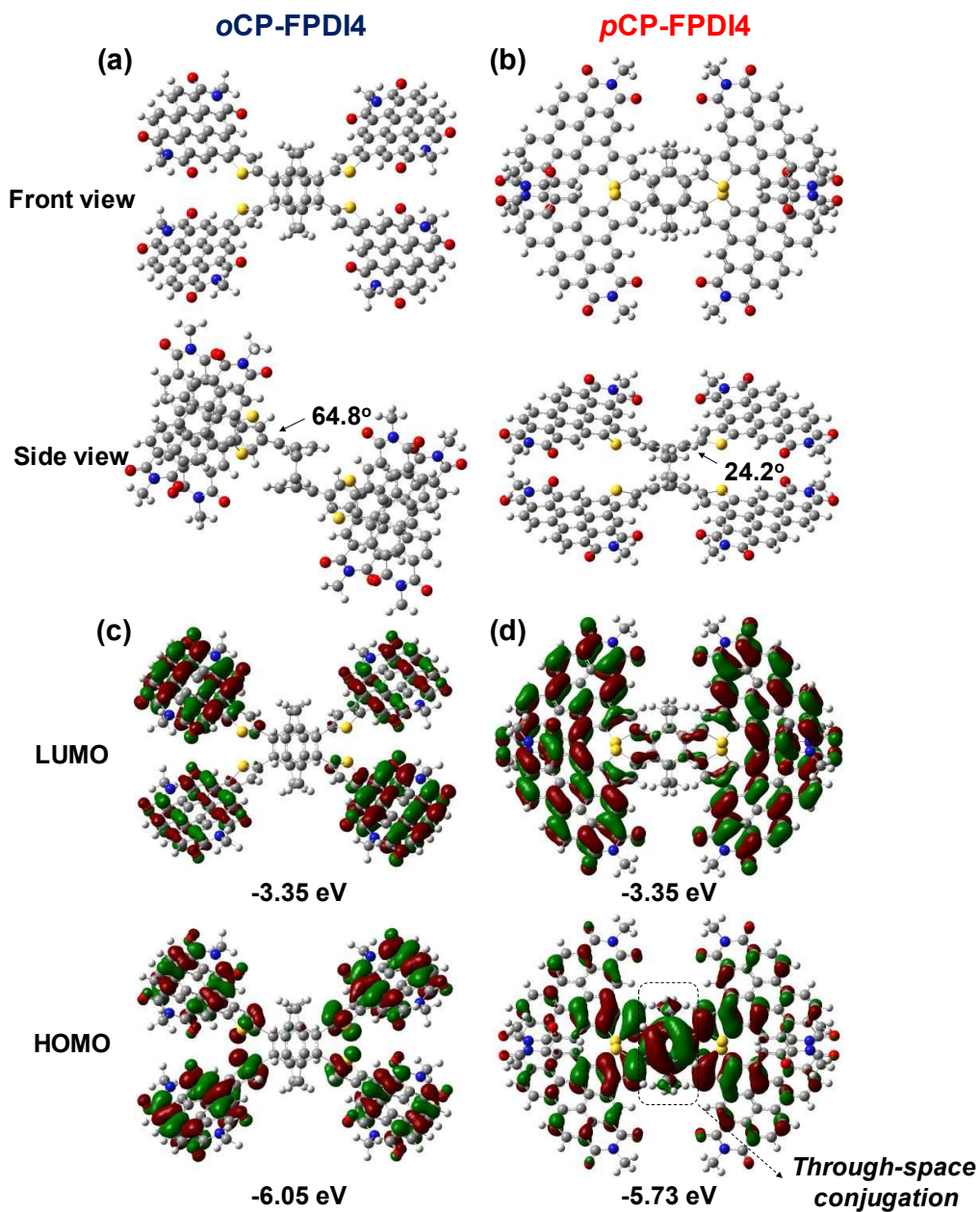
Figure 2. Optimized molecular geometry of (a) *o*CP-FPDI4 and (b) *p*CP-FPDI4 and frontier molecular orbitals of (c) *o*CP-FPDI4 and (d) *p*CP-FPDI4 calculated at the B3LYP/6-31+(d,p) level.

As depicted in **Figure 3a**, the UV-Vis absorption spectra of *o*CP-FPDI4 and *p*CP-FPDI4 were recorded in diluted solution state with a concentration of 1×10^{-5} M. *o*CP-

FPDI4 exhibits an absorption peak centered at 501 nm with an extinction coefficient of 1.68×10^5 M^{-1}cm^{-1}, while pCP-FPDI4 shows a slightly hypsochromic absorption peak centered at 493 nm with an extinction coefficient of 1.79×10^5 M^{-1}cm^{-1}. Interestingly, there is a shoulder peak appearing at ~520 nm in the spectrum of pCP-FPDI4, which is not seen in that of oCP-FPDI4. This shoulder peak can be assigned as HOMO-LUMO excitation from [2.2]paracyclophane to PDI, which can also be observed for PDI acceptors with strong intramolecular charge transfer features in literature.[7, 52, 53] Upon excitation at 500 nm, the photoluminescence spectra of oCP-FPDI4 and pCP-FPDI4 show broad and featureless peaks located at 547 and 597 nm, respectively. Therefore, bathochromic shifts in both absorption and emission spectra of pCP-FPDI4 are observed, suggesting its longer conjugation than oCP-FPDI4 as discussed above. In thin-film state, oCP-FPDI4 and pCP-FPDI4 exhibit absorption onsets of 544 and 590 nm, corresponding to optical bandgaps (E_g) of 2.31 and 2.18 eV, respectively. Both oCP-FPDI4 and pCP-FPDI4 can form complementary absorption when blended with P3TEA, covering the solar spectrum in the range of 300-750 nm (**Figure S2**). Regarding the electrochemical properties, cyclic voltammetry (CV, **Figure 3c**) measurements in film state were conducted to estimate the energy levels of the SMAs. As shown in **Figure 3d**, the LUMO levels of oCP-FPDI4 and pCP-FPDI4 were calculated to be -3.63 eV, which is close to that of P3TEA (-3.56 eV). Therefore, it is expected that the energetic offsets between P3TEA and these two SMAs should be very small, and the V_{OC} of the devices would be high.
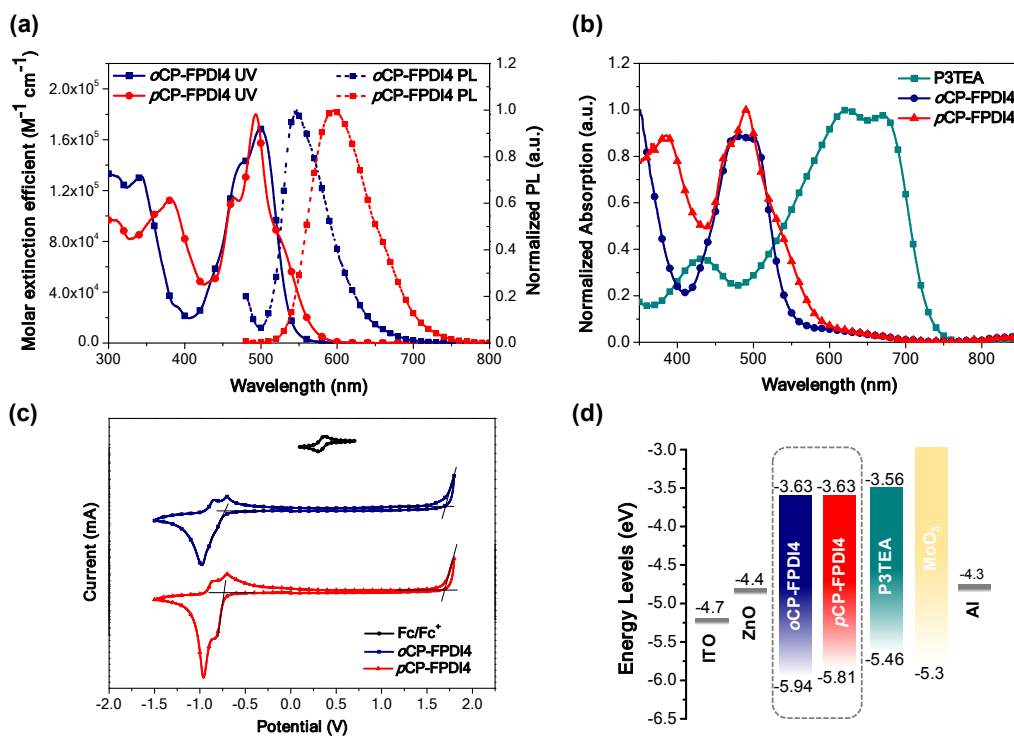
Figure 3. (a) UV-Vis absorption spectra of *o*CP-FPDI4 and *p*CP-FPDI4 in diluted chloroform solutions with a concentration of 1×10^{-5} M. (b) Normalized UV-Vis absorption spectra of P3TEA, *o*CP-FPDI4 and *p*CP-FPDI4 in the thin-film state. (c) Cyclic voltammetry curves of *o*CP-FPDI4 and *p*CP-FPDI4. (d) Energy alignment of P3TEA, *o*CP-FPDI4 and *p*CP-FPDI4.

Table 1. Optical and electrochemical properties of *o*CP-FPDI4 and *p*CP-FPDI4.

	T_d	$\lambda_{max,sol}$	$\lambda_{em,sol}$	$\alpha_{max,sol}$	$\lambda_{max,film}$	E_g [a]	LUMO[b]	HOMO[c]
	[°C]	[nm]	[nm]	[M⁻¹ cm⁻¹]	[nm]	[eV]	[eV]	[eV]
*o*CP-FPDI4	306	500	547	1.68×10^5	483	2.31	-3.63	-5.94
*p*CP-FPDI4	306	493	598	1.79×10^5	493	2.18	-3.63	-5.81

[a] calculated from the absorption onset of the films.

[b] estimated from the reduction onset of the CV curves.

[c] estimated by LUMO-E_g.

Table 2. Photovoltaic parameters of the solar cell devices based on P3TEA:oCP-FPDI4

and P3TEA:pCP-FPDI4 with the inverted structure under illumination of 100 mW/cm^2..

Material combinations	V_{OC} (V)	J_{SC} (mA/cm^2)	FF (%)	PCE (%)	μ_h/μ_e (cm^2/Vs)
P3TEA: pCP-FPDI4	1.16±0.01	13.47±0.37	56±1	8.76±0.14 (9.06)	2.1×10^{-4}/ 1.8×10^{-4}
P3TEA: oCP-FPDI4	1.17±0.02	5.88±0.25	33±1	2.29±0.17 (2.42)	8.4×10^{-5}/ 1.1×10^{-6}

[a] Average values from 20 devices with the highest values shown in parentheses.

To investigate the photovoltaic performances of the two polymers, PSCs were fabricated with the inverted device structure of indium tin oxide (ITO)/ZnO/BHJ/MoO$_3$/Al. The current density versus voltage (J-V) curves of the devices based on P3TEA:oCP-FPDI4 and P3TEA:pCP-FPDI4 are displayed in **Figure 4a**, and the photovoltaic parameters of the optimized devices are summarized in **Table 2.** Both material combinations generate remarkably high V_{OC} of 1.17 and 1.16 V for the P3TEA:oCP-FPDI4 and P3TEA:pCP-FPDI4 devices, respectively. As the optical bandgap of P3TEA is calculated to be 1.66 eV from its thin-film absorption onset, the voltage losses (defined as $V_{loss} = E_g/q$ -V_{OC}) based on the oCP-FPDI4 and pCP-FPDI4 systems are derived to be 0.49 and 0.50 V, respectively, which are among the lowest for PDI-based OSCs. Despite the comparable V_{OC}, these two devices show dramatic differences in J_{SC} and FF. The J_{SC} of the pCP-FPDI4-based devices is 2.3 times higher than that of the oCP-FPDI4-based ones (13.47 vs. 5.88 mA/cm^2). In addition, the FF of the oCP-FPDI4-based devices is only 33%, which is also inferior to that of the pCP-FPDI4-based ones (56%). As a result, the P3TEA:pCP-FPDI4 devices exhibit the

highest PCE of 9.06% owing to the simultaneously improved J_{SC} and FF, while the P3TEA:oCP-FPDI4 ones show the highest PCE of only 2.42%. Moreover, we tested the shelf life stability of the encapsulated devices based on the two PDI acceptors, both showed good stability as shown in **Figure S3**.

To verify the difference in J_{SC} between the oCP-FPDI4 and pCP-FPDI4-based devices, the external quantum efficiency (EQE) spectra based on the two blends were recorded. As shown in **Figure 4b**, the shapes of both EQE curves are similar with a broad light response in the range of 300-750 nm. The maximum EQE value is only 32% for the P3TEA:oCP-FPDI4 blend, while significant enhancement of EQE response of up to 68% was achieved by the P3TEA:pCP-FPDI4 one. Consequently, the integrated J_{SC} of the pCP-FPDI4-based blend is much higher than that of the oCP-FPDI4-based one (13.11 vs. 6.01 mA/cm^2), and this is consistent with the J_{SC} attained from the J-V characteristic curves. Furthermore, photoluminescence quenching experiments were performed to evaluate the charge dissociation process based on these two blends. Lasers with the wavelengths of 514 and 633 nm were chosen to excite the PDI-based molecules and P3TEA, respectively. As shown in **Figure S4**, the quenching efficiency of the P3TEA:pCP-FPDI4 blend relative to the pristine P3TEA film are much higher than that of the P3TEA:oCP-FPDI4 one (85.0% vs. 46.4%). Similar situations were also observed in the comparisons between the blend films and the pristine PDI-based films, where the quenching efficiencies of the pCP-FPDI4 and oCP-FPDI4-based systems were calculated to be 87.7% and 66.7%, respectively. Therefore, the photoluminescence quenching experiments suggest that the P3TEA:pCP-FPDI4 blend showcases more efficient hole as well as electron transfer processes, contributing to the higher J_{SC} of the devices.

The remarkable differences in J_{SC} and FF of the oCP-FPDI4 and pCP-FPDI4-based devices are further investigated by the charge recombination experiments. **Figure 4c** and **4d** show the results of the light-intensity-dependent J_{SC} and V_{OC} measurements. The relationship between J_{SC} and light intensity (P) can be described as $J_{SC} \propto P^\alpha$. If α

(the slope of the curve) reaches 1, it implies that the bimolecular recombination is effectively suppressed. The α values of the oCP-FPDI4 and pCP-FPDI4-based blends are calculated to be 0.96 and 0.98, respectively, indicating that the pCP-FPDI4-based blend exhibits weaker bimolecular recombination. Moreover, **Figure 4d** depicts the semi-logarithmic plots of the light-intensity-dependent V_{OC} experiments based on these two systems. The slopes extracted from the plots are 1.78 kT/q and 1.18 kT/q for the P3TEA:oCP-FPDI4 and P3TEA:pCP-FPDI4 devices, respectively, where k is the Boltzmann constant, T is the absolute temperature and q is the elementary charge. A slope larger than kT/q, indicating a stronger dependence of V_{OC} on the light intensity, can be observed if more trap-assisted recombination occurs. In other words, the pCP-FPDI4-based device shows less trap-assisted recombination than the pCP-FPDI4-based one. Therefore, both light-intensity-dependent experiments demonstrate more effectively suppressed charge recombination in the P3TEA:pCP-FPDI4 blend, which can partly explain the higher J_{SC} as well as FF achieved by this material combination.
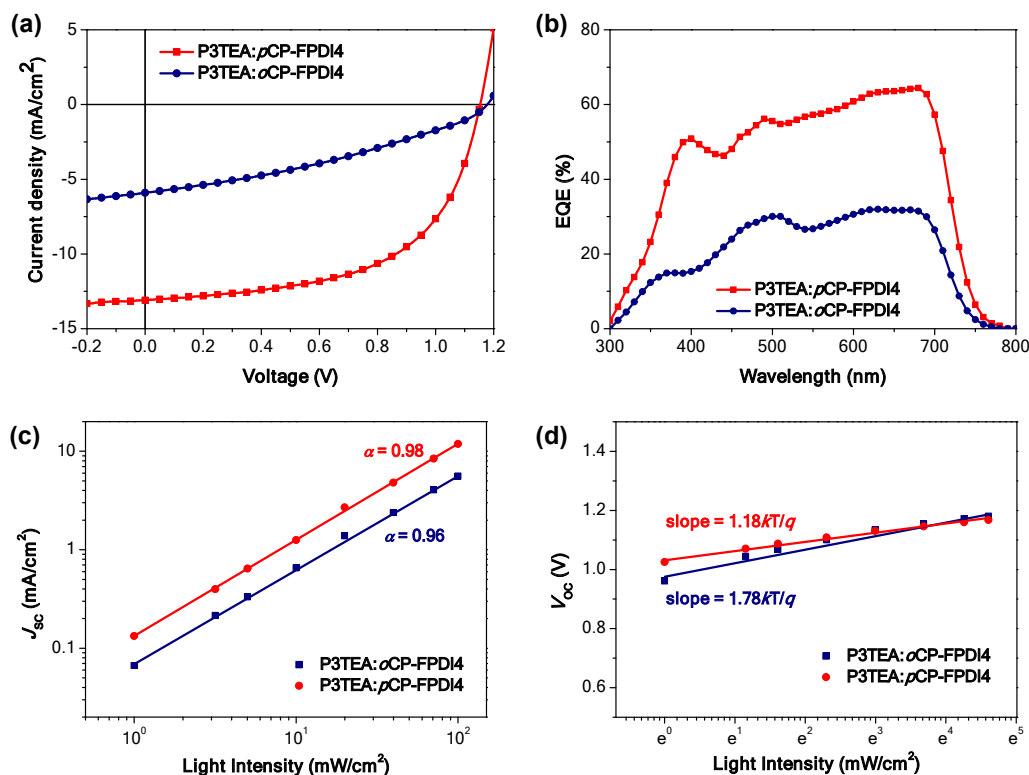

Figure 4. (a) J-V characteristics, (b) EQE spectra, (c) Light-intensity-dependent J_{SC}

plots and (d) Light-intensity-dependent V_{OC} plots of the P3TEA:oCP-FPDI4 and P3TEA:pCP-FPDI4 devices.

Grazing incidence wide-angle X-ray scattering (GIWAXS) measurement were carried out to provide insights into the molecular packing of oCP-FPDI4 and pCP-FPDI4. **Figure 5** displays the two-dimensional GIWAXS patterns and the corresponding one-dimensional line-cut scattering profiles in the in-plane (black line) and out-of-plane (red line) directions of the pristine and blend films. The (010) or π-π stacking peaks of the pristine oCP-FPDI4 and pCP-FPDI4 films are located at 1.45 and 1.47 Å^{-1}, respectively, corresponding to a π-π stacking distance of 4.26 and 4.33 Å. In the blend films, both systems exhibit predominant face-on orientation with the π-π stacking peaks of P3TEA located at 1.74 Å^{-1}. The (010) coherence lengths of P3TEA are extracted to be 28.94 and 36.94 Å when blended with oCP-FPDI4 and pCP-FPDI4, respectively, which is in agreement with the hole mobilities (μ_h: 8.4×10^{-5} vs. 2.1×10^{-4} cm^2/Vs) measured by the space-charge-limited current (SCLC, **Figure S5**) method. Interestingly, although the coherence length of oCP-FPDI4 is slightly larger than that of pCP-FPDI4 (12.54 vs. 8.69 Å), oCP-FPDI4 show electron mobilities that are two orders of magnitude lower than pCP-FPDI4 (μ_e: 1.1×10^{-6} vs. 1.8×10^{-4} cm^2/Vs). As a result, the P3TEA:pCP-FPDI4 device exhibits higher charge mobilities, as well as more balanced hole/electron charge transport, than the P3TEA:oCP-FPDI4 one, which accounts for the higher FF of pCP-FPDI4-based systems.

To figure out the reason for the marked contrast in charge dissociation and transport between the oCP-FPDI4 and pCP-FPDI4-based systems, resonant soft X-ray scattering (RSoXS) techniques were adopted to study the nano-scale phase segregation of these two blends. The Lorentz-corrected RSoXS profiles of the P3TEA:oCP-FPDI4 and P3TEA:pCP-FPDI4 blend films acquired at 285.8 eV are shown in **Figure 6**. The domain spacing of the P3TEA:pCP-FPDI4 blend is 22.02 nm, which is in the optimal range of 20-40 nm for OSC operations. On the contrary, the RSoXS profile of the

P3TEA:*o*CP-FPDI4 shifts to a lower *q*, indicating a larger domain spacing of 89.18 nm. The surprisingly large domain spacing of the P3TEA:*o*CP-FPDI4 blend severely deviates from the optimal range, which can well explain its low EQE response, photoluminescence quenching efficiency and electron mobility mentioned above. The larger phase segregation of the P3TEA:*o*CP-FPDI4 blend is also reflected by the atomic force microscopy (AFM, **Figure S6**) images, where the *o*CP-FPDI4-based blend shows a rougher surface morphology than the *p*CP-FPDI4-based one.
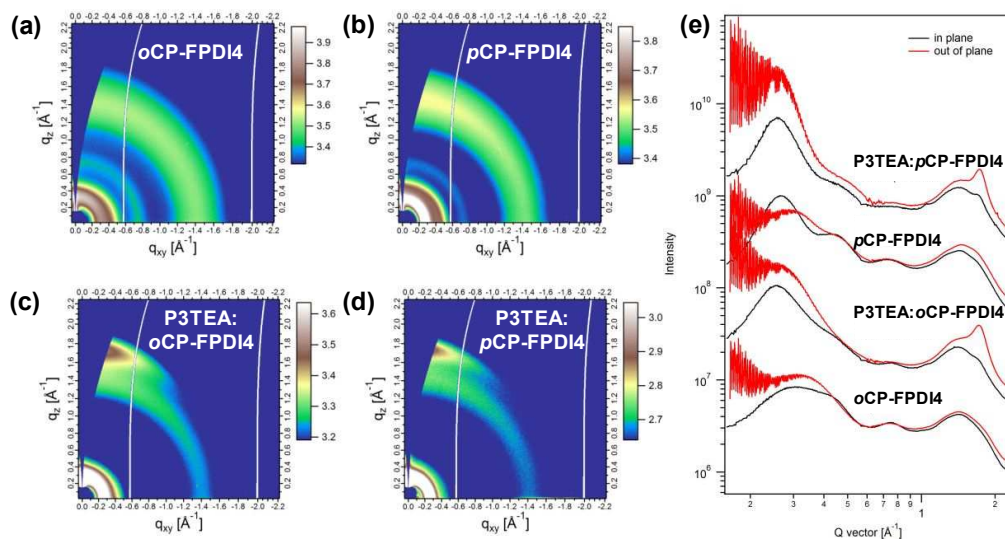
Figure 5. 2D GIWAXS patterns of (a) the pristine *o*CP-FPDI4 film, (b) the pristine *p*CP-FPDI4 film, (c) the P3TEA:*o*CP-FPDI4 blend film, (d) the P3TEA:*o*CP-FPDI4 blend film, and (e) the corresponding 1D GIWAXS profiles of the in-plane and out-of-plane directions.
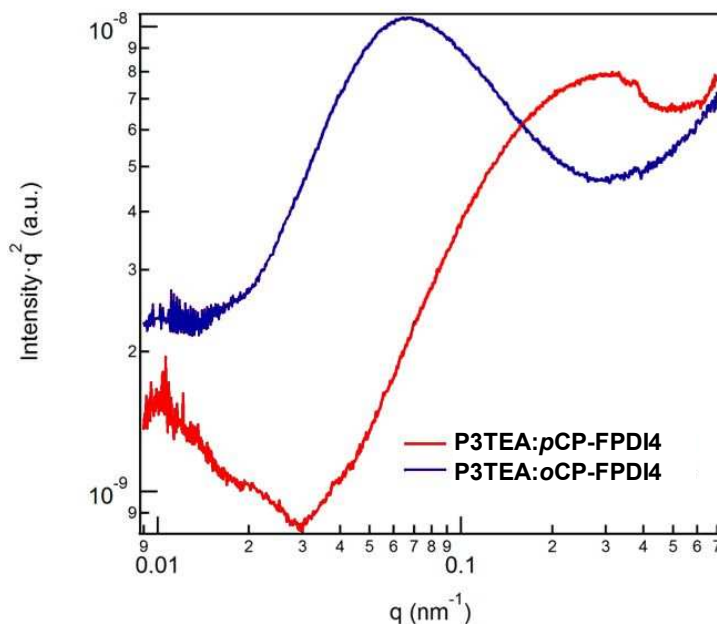
Figure 6. Lorentz-corrected RSoXS profiles of the P3TEA:*o*CP-FPDI4 and P3TEA:*p*CP-FPDI4 blend films acquired at 285.8 eV.

3. Conclusions

In summary, we designed and synthesized two isomeric PDI-based SMAs based on a novel [2.2]paracyclophane core for non-fullerene OSC operations. Due to the variations in the functionalization positions on the [2.2]paracyclophane moiety, *o*CP-FPDI4 and *p*CP-FPDI4 exhibits different molecular geometry and absorption properties. More importantly, the comparisons in their blend film morphology with P3TEA revealed that the P3TEA:*p*CP-FPDI4 blend formed suitable nano-scale phase segregation, thus leading to a lower extent of charge recombination and more efficient charge dissociation. Consequently, the P3TEA:*p*CP-FPDI4 devices obtained the highest PCE of 9.06% with a high V_{OC} of 1.16 V and a small voltage loss of 0.50 eV, which was far superior to the P3TEA:*o*CP-FPDI4 ones (2.42 %). The dramatic differences in photovoltaic performances between *o*CP-FPDI4 and *p*CP-FPDI4 highlight the importance of regulating the spatial orientations in the further molecular design of cyclophane-based SMAs to achieve the optimal absorption, electrical and morphological properties for OSCs.

Conflicts of interest

The authors declare no competing financial interests.

Reference

1.   J. Q. Zhang, H. S. Tan, X. G. Guo, A. Facchetti and H. Yan, *Nat. Energy*, 2018, **3**, 720-731.

2.   J. Hou, O. Inganas, R. H. Friend and F. Gao, *Nat Mater*, 2018, **17**, 119-128.

3.   C. Yan, S. Barlow, Z. Wang, H. Yan, A. K. Y. Jen, S. R. Marder and X. Zhan, *Nat. Rev. Mater.*, 2018, **3**, 18003.

4.   P. Cheng, G. Li, X. W. Zhan and Y. Yang, *Nat. Photon.*, 2018, **12**, 131-142.

5.   A. Wadsworth, M. Moser, A. Marks, M. S. Little, N. Gasparini, C. J. Brabec, D. Baran and I. McCulloch, *Chem Soc Rev*, 2019, **48**, 1596-1625.

6.   G. Zhang, J. Zhao, P. C. Y. Chow, K. Jiang, J. Zhang, Z. Zhu, J. Zhang, F. Huang and H. Yan, *Chem Rev*, 2018, **118**, 3447-3507.

7.   J. Zhang, Y. Li, J. Huang, H. Hu, G. Zhang, T. Ma, P. C. Y. Chow, H. Ade, D.

Pan and H. Yan, *J. Am. Chem. Soc.*, 2017, **139**, 16092-16095.

8.   W. Zhao, S. Li, H. Yao, S. Zhang, Y. Zhang, B. Yang and J. Hou, *J. Am. Chem. Soc.*, 2017, **139**, 7148-7151.

9.   Y. Zhong, M. T. Trinh, R. Chen, G. E. Purdum, P. P. Khlyabich, M. Sezen, S. Oh, H. Zhu, B. Fowler, B. Zhang, W. Wang, C. Y. Nam, M. Y. Sfeir, C. T. Black, M. L. Steigerwald, Y. L. Loo, F. Ng, X. Y. Zhu and C. Nuckolls, *Nat Commun*, 2015, **6**, 8242.

10.   Y. Z. Lin, Z. G. Zhang, H. T. Bai, J. Y. Wang, Y. H. Yao, Y. F. Li, D. B. Zhu and X. W. Zhan, *Energy Environ. Sci.*, 2015, **8**, 610-616.

11.   H. Yao, Y. Cui, R. Yu, B. Gao, H. Zhang and J. Hou, *Angew Chem Int Ed Engl*, 2017, **56**, 3045-3049.

12.   L. Meng, Y. Zhang, X. Wan, C. Li, X. Zhang, Y. Wang, X. Ke, Z. Xiao, L. Ding, R. Xia, H. L. Yip, Y. Cao and Y. Chen, *Science*, 2018, **361**, 1094-1098.

13.   H. Zhang, H. Yao, J. Hou, J. Zhu, J. Zhang, W. Li, R. Yu, B. Gao, S. Zhang and J. Hou, *Adv. Mater.*, 2018, **30**, e1800613.

14.   F. Wurthner, C. R. Saha-Moller, B. Fimmel, S. Ogi, P. Leowanawat and D. Schmidt, *Chem Rev*, 2016, **116**, 962-1052.

15.   T. Weil, T. Vosch, J. Hofkens, K. Peneva and K. Mullen, *Angew Chem Int Ed Engl*, 2010, **49**, 9068-9093.

16.   X. Guo, A. Facchetti and T. J. Marks, *Chem Rev*, 2014, **114**, 8943-9021.

17.   X. Zhan, A. Facchetti, S. Barlow, T. J. Marks, M. A. Ratner, M. R. Wasielewski and S. R. Marder, *Adv. Mater.*, 2011, **23**, 268-284.

18.   Y. Lin, Y. Wang, J. Wang, J. Hou, Y. Li, D. Zhu and X. Zhan, *Adv. Mater.*, 2014, **26**, 5137-5142.

19.   X. Zhang, Z. Lu, L. Ye, C. Zhan, J. Hou, S. Zhang, B. Jiang, Y. Zhao, J. Huang, S. Zhang, Y. Liu, Q. Shi, Y. Liu and J. Yao, *Adv. Mater.*, 2013, **25**, 5791-5797.

20.   S. Y. Liu, C. H. Wu, C. Z. Li, S. Q. Liu, K. H. Wei, H. Z. Chen and A. K. Jen, *Adv Sci (Weinh)*, 2015, **2**, 1500014.

21.   A. Zhang, C. Li, F. Yang, J. Zhang, Z. Wang, Z. Wei and W. Li, *Angew Chem*

Int Ed Engl, 2017, **56**, 2694-2698.

22.   Q. F. Yan, Y. Zhou, Y. Q. Zheng, J. Pei and D. H. Zhao, *Chem. Sci.*, 2013, **4**, 4389-4394.

23.   Y. Liu, C. Mu, K. Jiang, J. Zhao, Y. Li, L. Zhang, Z. Li, J. Y. Lai, H. Hu, T. Ma, R. Hu, D. Yu, X. Huang, B. Z. Tang and H. Yan, *Adv. Mater.*, 2015, **27**, 1015-1020.

24.   H. Lin, S. Chen, H. Hu, L. Zhang, T. Ma, J. Y. Lai, Z. Li, A. Qin, X. Huang, B. Tang and H. Yan, *Adv. Mater.*, 2016, **28**, 8546-8551.

25.   J. B. Zhao, Y. K. Li, J. Q. Zhang, L. Zhang, J. Y. L. Lai, K. Jiang, C. Mu, Z. K. Li, C. L. C. Chan, A. Hunt, S. Mukherjee, H. Ade, X. H. Huang and H. Yan, *J. Mater. Chem. A*, 2015, **3**, 20108-20112.

26.   Y. Duan, X. Xu, H. Yan, W. Wu, Z. Li and Q. Peng, *Adv. Mater.*, 2017, **29**, 1605115.

27.   Q. Wu, D. Zhao, A. M. Schneider, W. Chen and L. Yu, *J. Am. Chem. Soc.*, 2016, **138**, 7248-7251.

28.   G. Zhang, X. Xu, Y. W. Lee, H. Y. Woo, Y. Li and Q. Peng, *Adv. Funct. Mater.*, 2019, **29**, 1906587.

29.   S. Yu, Y. Chen, J. Wu, D. Xia, S. Hong, X. Wu, J. Yu, S. Zhang, A. Peng and H. Huang, *ACS Appl Mater Interfaces*, 2018, **10**, 28812-28818.

30.   S. M. McAfee, S. V. Dayneko, A. D. Hendsbee, P. Josse, P. Blanchard, C. Cabanetos and G. C. Welch, *J. Mater. Chem. A*, 2017, **5**, 11623-11633.

31.   T. Huang, H. Chen, J. Feng, A. Zhang, W. Jiang, F. He and Z. Wang, *ACS Materials Lett.*, 2019, **1**, 404-409.

32.   P. E. Hartnett, H. Matte, N. D. Eastham, N. E. Jackson, Y. Wu, L. X. Chen, M. A. Ratner, R. P. H. Chang, M. C. Hersam, M. R. Wasielewski and T. J. Marks, *Chem Sci*, 2016, **7**, 3543-3555.

33.   Y. Zhong, M. T. Trinh, R. Chen, W. Wang, P. P. Khlyabich, B. Kumar, Q. Xu, C. Y. Nam, M. Y. Sfeir, C. Black, M. L. Steigerwald, Y. L. Loo, S. Xiao, F. Ng, X. Y. Zhu and C. Nuckolls, *J. Am. Chem. Soc.*, 2014, **136**, 15215-15221.

34. B. Wang, W. Q. Liu, H. B. Li, J. Q. Mai, S. Y. Liu, X. H. Lu, H. Y. Li, M. M. Shi, C. Z. Li and H. Z. Chen, *J. Mater. Chem. A*, 2017, **5**, 9396-9401.

35. D. J. Walwark, B. D. Datko, Q. H. Wu, A. Neshchadin, M. L. Berrens, L. P. Yu and J. K. Grey, *J. Phys. Chem. C*, 2018, **122**, 23261-23270.

36. H. Zhong, C. H. Wu, C. Z. Li, J. Carpenter, C. C. Chueh, J. Y. Chen, H. Ade and A. K. Jen, *Adv. Mater.*, 2016, **28**, 951-958.

37. D. Meng, H. Fu, C. Xiao, X. Meng, T. Winands, W. Ma, W. Wei, B. Fan, L. Huo, N. L. Doltsinis, Y. Li, Y. Sun and Z. Wang, *J. Am. Chem. Soc.*, 2016, **138**, 10184-10190.

38. H. W. Hu, Y. K. Li, J. Q. Zhang, Z. X. Peng, L. K. Ma, J. M. Xin, J. C. Huang, T. X. Ma, K. Jiang, G. Y. Zhang, W. Ma, H. Ade and H. Yan, *Adv. Energy Mater.*, 2018, **8**, 1800234.

39. Q. H. Wu, D. L. Zhao, J. H. Yang, V. Sharapov, Z. Cai, L. W. Li, N. Zhang, A. Neshchadin, W. Chen and L. P. Yu, *Chem. Mater.*, 2017, **29**, 1127-1133.

40. H. Sun, X. Song, J. Xie, P. Sun, P. Gu, C. Liu, F. Chen, Q. Zhang, Z. K. Chen and W. Huang, *ACS Appl Mater Interfaces*, 2017, **9**, 29924-29931.

41. J. Zhang, F. Bai, Y. Li, H. Hu, B. Liu, X. Zou, H. Yu, J. Huang, D. Pan, H. Ade and H. Yan, *J. Mater. Chem. A*, 2019, **7**, 8136-8143.

42. G. Zhang, J. Feng, X. Xu, W. Ma, Y. Li and Q. Peng, *Adv. Funct. Mater.*, 2019, **29**, 1906587.

43. J. Li, P. Shen, Z. Zhao and B. Z. Tang, *CCS Chemistry*, 2019, **1**, 181-196.

44. P. G. Ghasemabadi, T. Yao and G. J. Bodwell, *Chem Soc Rev*, 2015, **44**, 6494-6518.

45. K. J. Weiland, A. Gallego and M. Mayor, *Eur J Org Chem*, 2019, **2019**, 3073-3085.

46. M. Bai, J. Liang, L. Xie, S. Sanvito, B. Mao and S. Hou, *J Chem Phys*, 2012, **136**, 104701.

47. Y. Morisaki and Y. Chujo, *Polym. Chem.*, 2011, **2**, 1249-1257.

48. S. P. Jagtap and D. M. Collard, *J. Am. Chem. Soc.*, 2010, **132**, 12208-12209.

49.   S. Mukhopadhyay, S. P. Jagtap, V. Coropceanu, J. L. Bredas and D. M. Collard, *Angew Chem Int Ed Engl*, 2012, **51**, 11629-11632.

50.   Y. Morisaki, N. Kawakami, T. Nakano and Y. Chujo, *Chem. Eur. J.*, 2013, **19**, 17715-17718.

51.   J. L. Zafra, A. Molina Ontoria, P. Mayorga Burrezo, M. Pena-Alvarez, M. Samoc, J. Szeremeta, F. J. Ramirez, M. D. Lovander, C. J. Droske, T. M. Pappenfus, L. Echegoyen, J. T. Lopez Navarrete, N. Martin and J. Casado, *J. Am. Chem. Soc.*, 2017, **139**, 3095-3105.

52.   S. X. Li, W. Q. Liu, C. Z. Li, T. K. Lau, X. H. Lu, M. M. Shi and H. Z. Chen, *J. Mater. Chem. A*, 2016, **4**, 14983-14987.

53.   N. J. Schuster, D. W. Paley, S. Jockusch, F. Ng, M. L. Steigerwald and C. Nuckolls, *Angew Chem Int Ed Engl*, 2016, **55**, 13519-13523.